

# Enabling Increased Delithiation Rates in Silicon-Based Anodes through Alloying with Phosphorus

Frederik T. Huld,<sup>\*[a, c]</sup> Samson Y. Lai,<sup>[b]</sup> Wakshum M. Tucho,<sup>[d]</sup> Rasim Batmaz,<sup>[a]</sup> Ingvild T. Jensen,<sup>[e, f]</sup> Song Lu,<sup>[c]</sup> Obinna E. Eleri,<sup>[a, c]</sup> Alexey Y. Koposov,<sup>\*[b, e]</sup> Zhixin Yu,<sup>\*[c]</sup> and Fengliu Lou<sup>\*[a]</sup>

The capability of battery materials to deliver not only high lithium storage capacity, but also the ability to operate at high charge/discharge rates is an essential property for development of new batteries. In the present work, the influence on the charge/discharge rate behaviour of substoichiometric concentrations of phosphorus (P) in silicon (Si) nanoparticles was studied. The results revealed an increase in rate capability as a function of the P concentration between 0 and 5.2 at%, particularly during delithiation. The stoichiometry of the nano-

particles was found to strongly affect the formation of the  $\text{Li}_{3.5}\text{Si}$  phase during lithiation. Cyclic stability experiments demonstrated an initial increase in capacity for the  $\text{SiP}_x$  materials. Galvanostatic intermittent titration technique and electrochemical impedance spectroscopy demonstrated the increased lithium diffusivity with inclusion of P. Density functional theory and *ab initio* molecular dynamics were deployed to provide a rationale for the electrochemical behaviour of  $\text{SiP}_x$ .

## Introduction

Li-ion batteries (LIBs) are one of the most used energy storage devices due to their relatively high energy storage capacity, an ability to operate under high charge/discharge rates, and possibility for small size and portability.<sup>[1]</sup> As requirements for LIBs continue to grow, design and research into new active

materials for LIBs have become necessary to enable the delivery of high power and improvement of energy storage capacity. Much of the recent work has been focussed on optimizing the properties of silicon (Si) as an anode material, due to its ten-fold greater Li-ion storage capacity compared to conventionally used graphite.<sup>[2–4]</sup> However, the volume change of Si during lithiation/delithiation is also much greater than for graphite (300% vs 10%), which leads to fracturing of Si particles, delamination of the active materials from the current collector, and unstable solid electrolyte interphase (SEI) formation. All of these factors lead to rapid degradation of Si-based electrodes during electrochemical cycling.<sup>[5–7]</sup> In addition, the diffusivity of  $\text{Li}^+$  ions in Si is also lower than that in graphite ( $10^{-10}$  vs  $10^{-7}$   $\text{cm}^2/\text{s}$ ).<sup>[8,9]</sup> Low diffusivity of  $\text{Li}^+$  inside Si, as well as high charge-transfer resistance at the surface contribute to the low rate capability, which impedes the use of Si in high power applications.<sup>[2–4]</sup>

More than a decade of work has been dedicated to mitigating the effects of the volume change in Si and other materials operating through alloying mechanism. This has been approached through the use of coatings, materials engineering, and/or by nanostructuring of Si.<sup>[10–13]</sup> Alternatively, Si-based alloys and substoichiometric compounds have been proposed to change the cycling behaviour of Si,<sup>[14–17]</sup> thereby improving the intrinsic properties in combination with extrinsic methods such as nanostructuring and/or coatings. In the search for improvement of the Si-based materials and synergetic affect between Si and heteroatoms, alternative strategies have been deployed including physical mixing of Si nanoparticles and layered black phosphorus.<sup>[18]</sup>

Recently, materials such as  $\text{SiO}_x$ ,  $\text{SiN}_x$  or  $\text{SiP}_x$  have shown great promise due to their incredible cycling stability originating from conversion/alloying mechanisms.<sup>[19–24]</sup> For  $\text{SiO}_x$ ,  $\text{SiN}_x$  and  $\text{SiP}_x$  with  $x < 1$ , it has been shown that the added element participates in the formation of an inactive matrix during initial

[a] F. T. Huld, Dr. R. Batmaz, O. E. Eleri, Dr. F. Lou  
Beyonder  
Stokkamyrvæien 30, N-4313 Sandnes, Norway  
E-mail: frederik@beyonder.no  
fengliu@beyonder.no


[b] Dr. S. Y. Lai, Prof. A. Y. Koposov  
Battery Technology Department  
Institutt for Energiteknikk  
2007 Kjeller, Norway


[c] F. T. Huld, S. Lu, O. E. Eleri, Prof. Z. Yu  
University of Stavanger  
4036, Stavanger, Norway  
E-mail: zhixin.yu@uis.no

[d] Dr. W. M. Tucho  
Department of Mechanical and Structural Engineering and Materials  
University of Stavanger  
4036, Stavanger, Norway

[e] Dr. I. T. Jensen, Prof. A. Y. Koposov  
Center for Materials Science and Nanotechnology  
Department of Chemistry  
P.O. Box 1033, Blindern, 0371 Oslo, Norway  
E-mail: Alexey.koposov@kjemi.uio.no

[f] Dr. I. T. Jensen  
Sustainable Energy Technology  
Sintef  
Forskningsveien 1NO- 0373 Oslo, Norway

 Supporting information for this article is available on the WWW under <https://doi.org/10.1002/slct.202202857>

 © 2022 The Authors. ChemistrySelect published by Wiley-VCH GmbH. This is an open access article under the terms of the Creative Commons Attribution License, which permits use, distribution and reproduction in any medium, provided the original work is properly cited.

lithiation, leaving domains of pure Si as the main source of reversible capacity.<sup>[2,19,25]</sup> The advantage of these materials is the high  $\text{Li}^+$  diffusivity through the inactive matrix and the substantial decrease in swelling compared to Si, which leads to an increase in both rate capability and stability during cycling. For instance, lithium phosphidosilicates (possible products of  $\text{SiP}_x$  conversion), which consist of Li, Si and P in various ratios, have been shown to have high  $\text{Li}^+$  ion mobility, which can increase the  $\text{Li}^+$  diffusivity of Si-based anodes.<sup>[26,27]</sup> However, the major disadvantage of relatively high concentrations of added element (*i.e.*, high  $x$ ) is a decreased initial Coulombic efficiency (ICE) due to the irreversible *in situ* conversion reaction.<sup>[2,19]</sup> In addition, the electrochemistry of Si-based alloys is not straightforward, as some of the elements used for alloying can react with  $\text{Li}^+$  to form Li–Si-containing compounds, complicating the data analysis and further improvement of these otherwise promising materials.<sup>[19,28]</sup> At the present moment the results for  $\text{SiNPs}$ ,<sup>[29,30]</sup>  $\text{SiO}_x$ ,<sup>[31–33]</sup>  $\text{SiP}_x$ <sup>[16,20,22,23,34–36]</sup> and  $\text{SiNx}$ <sup>[25]</sup> materials systems are still quite scattered in terms of methods of preparation, chemical compositions, particle morphologies and sizes (these are differences only at the material level) due to relative novelty of the approach. All of those discrepancies makes a direct comparison of these promising materials extremely difficult and more studies yet to be performed to develop a full understanding of these Si-based compounds.

Alternatively, the intrinsic properties of Si battery active materials can also be modified by doping. The aim of such doping is to provide a stabilization effect similar to the conversion/alloying mechanism observed at high  $x$ , but without decreasing ICE.<sup>[16,19,34–36]</sup> For instance, boron-doped Si nanoparticles were reported, but this doping was found not to improve the rate capability of the Si because boron (B) is a p-type dopant.<sup>[17]</sup> Conversely, n-type dopants, such as phosphorus (P) and arsenic (As) showed promising results for improvement of anode materials.<sup>[15,31,35–37]</sup> Furthermore, P-doped Si/graphite composites demonstrated good rate capabilities due to lower charge transfer resistance and improved  $\text{Li}^+$  transport in the material compared to pure Si.<sup>[35]</sup> P is a promising choice as an n-type dopant due to its lower toxicity compared to other candidates such as As. Depending on P concentration in Si (at doping or sub-stoichiometric levels),  $\text{SiP}_x$  is expected to maintain some of the advantages of doped Si—namely the increased conductivity relative to pure Si, but also possibly the advantages of conversion materials such as increased  $\text{Li}^+$  diffusivity and high cycling stability.

Previous work on substoichiometric  $\text{SiP}_x$  materials has shown the increase in both the conductivity and  $\text{Li}^+$  diffusivity of  $\text{SiP}_x$  at low P%.<sup>[34]</sup> However, the mechanism by which the addition of P affects the electrochemical behaviour is difficult to determine, as effects due to surface oxides and material nanostructuring play a significant role in the electrochemical behaviour. Figure 1 shows some  $\text{SiP}_x$  materials recently reported in the literature. This survey is displayed on a scale of the atomic % of P in the Si material used, which is divided into regions depending on the major mechanism attributed to

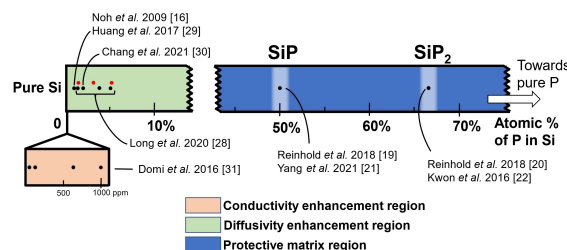


**Figure 1.** Schematic illustration showing present work on  $\text{SiP}_x$  anode materials displayed as a function of the atomic% of P in Si, as well as the main effect attributed to the P in the given concentration range. Our contribution is shown as off-set red circles.

material enhancements at that P%. The contribution of the current work is shown as offset red circles.

A silane pyrolysis process was used to disambiguate the effect of low concentrations of P in Si nanoparticles by synthesizing particles of very similar morphology and with low surface oxide levels.<sup>[25,31]</sup> In the present article, we describe the synthesis of amorphous  $\text{SiP}_x$  nanoparticles with the atomic % of phosphorus in the particles ranging from 1.5 to 5.2 at% and compare their electrochemical performance to pristine Si nanoparticles of the same size.

## Results and Discussion

### Materials characterisation of $\text{SiP}_x$ and Si NPs

Si-based materials obtained through the silane pyrolysis route typically give rise to amorphous nanoparticles (NPs) with relatively narrow size distribution.<sup>[31]</sup> This process conveniently allows for the preparation of nanoparticles with the target size and morphology through controlled nucleation and growth. The introduction of  $\text{PH}_3$  gas into  $\text{SiH}_4$  pyrolysis process resulted in the formation of  $\text{SiP}_x$  NPs, where the ratio of Si:P is manipulated through control of the ratio of silane to phosphine gases supplied into the reactor during pyrolysis. This technique has been previously applied not only to produce Si nanoparticles,<sup>[31]</sup> but also to produce more complex  $\text{SiN}_x$  (nano)particles with precise ratios of Si:N and controlled morphology and particle size.<sup>[25]</sup> The obtained materials were characterized using microscopy-based methods, as the amorphous nature of the  $\text{SiP}_x$  particles as well as the formation of a solid solution of P in Si limits the selection of characterization techniques. Transmission electron microscopy (TEM) images of the nanoparticles shows a distribution of partially aggregated particles, as illustrated in Figure 2a for P5.2. The microscopy characterization for materials P0, P1.5, and P3.2 is shown in Figure S1. These aggregates consist of primary particles with a radius below 50 nm, fused together in a branching pattern. These nanostructures are typical of Si nanomaterials prepared by  $\text{SiH}_4$  pyrolysis, and are much smaller than the critical size of 150 nm.<sup>[31,38–40]</sup> The distributions of primary particle sizes shown in histograms in Figure S2 illustrate a small decrease in primary particle radius with increasing P%. This difference is the most

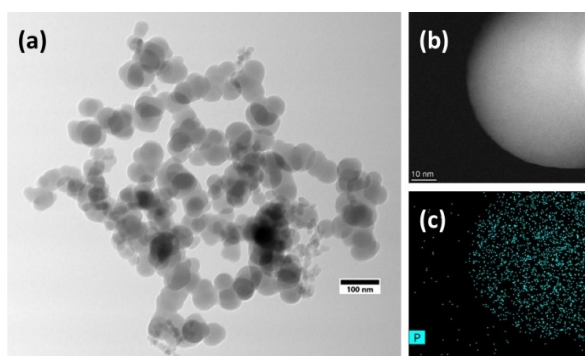


**Figure 2.** (a) TEM image showing a micron-sized aggregate of P5.2; (b) HAADF image of a single particle of the P5.2 material; (c) HAADF-EDS mapping of P in a particle of P5.2 material.

pronounced for pure Si, which shows an average particle radius  $\sim 10$  nm greater than the material with highest P content. The three  $\text{SiP}_x$  materials, however, show only a small variation in particle size distribution. The size of NPs is known to change the electrochemical properties, with larger particles showing an increase in overpotential.<sup>[41,42]</sup> However, we do not expect these small, highly overlapped differences to cause a significant difference in electrochemistry.

Figure 2b and 2c show HAADF and HAADF-EDS images of the P5.2 material, respectively. The lack of a bright “edge” around the particle in Figure 2c indicates that the P is not concentrated at the surface of the particle, but rather distributed evenly throughout. EDS spectra can be found in Figure S3 and show very low concentrations of oxygen on the particles. For an accurate determination of the stoichiometry, the atomic percentages of P were determined by ICP-OES and are shown in Table 1. Furthermore, X-ray diffraction (XRD) analysis (Figure S4) of the four materials confirmed their amorphous structure, with no peaks observed to indicate the presence of crystalline Si or measurable quantities of  $\text{SiP}/\text{SiP}_2$  phases.<sup>[21]</sup>

### Stability and rate capability of $\text{SiP}_x$ NPs

Galvanostatic charge-discharge (GCD) testing was performed in half-cells using Li foil as a counter electrode. The currents chosen for formation and subsequent tests were based on the capacity of the materials in order to minimise differences in stresses experienced by differing materials. This is also why

Table 1. Chemical and initial electrochemical parameters for the four Si-based materials prepared for the present study.			
Material name	P concentration (atomic %)	Capacity of 1 <sup>st</sup> lithiation ( $\text{mAhg}^{-1}$ )	ICE (%) <sup>[a]</sup>
P0	0	3,533	87.1 $\pm$ 0.6
P1.5	1.5	3,066	88 $\pm$ 2
P3.2	3.2	2,905	85 $\pm$ 1
P5.2	5.2	2,830	87.7 $\pm$ 0.3

[a] Errors were calculated from the average of three cells.

current densities are reported in C-rates (with units of  $\text{h}^{-1}$ ), instead of  $\text{mA g}^{-1}$ .

The 1<sup>st</sup> cycle charge-discharge curves for the studied materials are shown in Figure S5a. Table 1 summarizes the data from the 1<sup>st</sup> cycle, and includes the measured gravimetric capacity taken from the first lithiation step for each material, as well as the ICE. Table 1 shows that all the  $\text{SiP}_x$  materials have lower initial capacity than pristine Si. The change of capacity is not linear: P3.2 and P5.2 exhibiting similar initial capacities, while P1.5 has a higher capacity than other  $\text{SiP}_x$  samples. The similarity of the ICEs indicates that there is no appreciable formation of lithium phosphide ( $\text{Li}_3\text{P}$ ) or other matrix materials through any conversion reaction, as existence of such would cause the ICE to decrease as a function of the amount of P in the material. The capacities of the materials exhibit a strong negative dependence on the P%, which is greater than what would be expected from the theoretical reaction of  $\text{Si}_x\text{P}_{1-x} + (3 + 0.5x)\text{Li} \rightarrow x[\text{Li}_{3.5}\text{Si}] + (1-x)[\text{Li}_3\text{P}]$ . This is consistent with the results of other researchers, who have reported that the initial capacity of  $\text{Si}_x\text{P}_{1-x}$  is lower than expected values.<sup>[15,20,21,35]</sup> As the ICEs of all materials are very close and the conversion reaction can be neglected, it is possible to suggest that the formation of SEI is similar for all studied materials.

Figure S5b shows the first cycle differential capacity ( $dQ/dV$ ) plots of the studied materials. The  $\text{SiP}_x$  materials exhibit sharp peaks during lithiation below 0.3 V, which is common for the first cycle of Si. The formation of  $\text{Li}_3\text{P}$  at around 0.4 V expected from the literature has not been seen for any of the  $\text{SiP}_x$  materials studied in the present work.<sup>[21–23]</sup> The absence of distinctive features signalling the formation of lithium phosphosilicates or  $\text{Li}_3\text{P}$  are likely due to the low concentration of P in  $\text{SiP}_x$ . These species should account for less than 5% of the total capacity, and would, therefore, be lost in the much larger peaks corresponding to the formation of lithium silicide ( $\text{Li}_x\text{Si}$ ) and SEI. The two broad peaks in the delithiation step are characteristic for delithiation of the amorphous  $\alpha\text{-Li}_{3.5}\text{Si}$  and  $\alpha\text{-Li}_{2.0}\text{Si}$  phases.<sup>[43,44]</sup> The peaks that are expected for the conductive additives (mainly the conductive graphite) are too small to be visible due to the high (60% by weight) loading of Si-based material, and thus the electrochemical behaviour of the cells can be considered to be predominantly due to Si or  $\text{SiP}_x$ . The electrochemical testing was performed with the voltage cut-off was set to 0.05 V to avoid the formation of  $\text{c-Li}_{15}\text{Si}_4$  phase, which typically manifests itself by the presence of sharp peaks at 0.4 V in the delithiation curves – absent for the present materials.<sup>[42]</sup> Therefore, the advantages of forming a protective matrix with high  $\text{Li}^+$  diffusivity are not available for  $\text{SiP}_x$  at the studied range of P concentrations.

In order to study the charge/discharge behaviour of Si and Si-based materials, it is important to recognize the difference in electrochemical behaviour during lithiation and delithiation.<sup>[45]</sup> It is important to consider these processes separately when evaluating materials particularly at high charge/discharge rates.

Therefore, stability tests were carried out by lithiating and delithiating at asymmetric C-rates. The delithiation behaviour was studied by setting the delithiation rate to 0.3 C, and the lithiation rate to 0.1 C. This was done to reduce the stress on

the electrode during lithiation and allow any electrochemical processes to run to completion. In this way, the behaviour of a delithiation step was not limited by the preceding lithiation step. A diagnostic cycle – where both the lithiation and delithiation C-rate was set to 0.05 C – was included after every tenth cycle to explore the evolution of the overpotential. The lithiation-dependent stability was studied in the same manner, with a slow delithiation process at 0.1 C and a faster lithiation at 0.3 C. The stability during fast delithiation (Figure 3a) shows that the total capacity increases for SiP<sub>x</sub> materials after the initial formation (delimited by the vertical dashed line), but not for the pristine Si (P0). Gradual capacity increases are observed in other literature, but the reason is not completely understood.<sup>[25,46]</sup> For P0, P1.5 and P3.2 the difference between the cycling and diagnostic cycles remains unchanged, indicating that the overpotential is constant. In contrast, the disparity between the cycling and diagnostic cycles in P5.2 is larger at later cycles, which implies that the overpotential increases over time. By the 40<sup>th</sup> cycle, all the materials dropped below 80% of their capacity relative to the first cycle after formation (the 1<sup>st</sup> cycle after the dashed line). An example of the capacity retention of SiP<sub>x</sub> full cells is given in figure S6, to demonstrate the behaviour in a different system.

The lithiation-dependent performance was studied in the same manner, with a slow delithiation process at 0.1 C and a faster lithiation at 0.3 C. The performance of the materials as a function of lithiation is shown in Figure 3b. Here the capacity increase is also observed. The relatively large lithiation current means that the potential limit is reached before full lithiation of the active material is achieved. This explains why the number

of cycles required to reach the maximum capacity is greater than that observed in Figure 3a. The difference in capacity between the fast cycles and the diagnostic cycles is more or less constant for the SiP<sub>x</sub> materials, indicating that the overpotential is consistent with repeated cycling. For P0, the small decrease in this difference indicates that the overpotential is decreasing slightly.

Rate capability tests were performed in a similar manner to the stability tests, i.e. by lithiating the electrodes at 0.1 C and delithiating at increasing rates (or *vice versa*). The data is normalized to the first point after formation (marked with a star) to highlight the relative rate behaviour of the materials. Figure 3c shows that the delithiation capacity is mostly independent of the applied current (within the chosen current range), and that the loss of capacity is due to aging in the same way as the stability behaviour seen in Figure 3a. Figure 3d, however, shows a strong relationship between the lithiation capacity of the electrodes and the applied current. Here, the SiP<sub>x</sub> materials show slightly better capacity retention in the 0.1–0.7 C range compared to the pure Si, but at 1 C P1.5 and P3.2 perform worse than the pristine Si. The capacity is recovered once the applied current returns to C-rates below this inflection point, allowing us to conclude that this capacity loss is not due to cell failure or aging. From this we can conclude that lithiation is the limiting factor in determining the rate capability of Si nanoparticles.

Analysis of the evolution of dQ/dV plots can provide additional insights to the differences in behaviour between the materials, explaining both the rate capabilities and the initial increase of capacities for SiP<sub>x</sub> during cycling. Figures 4 and 5

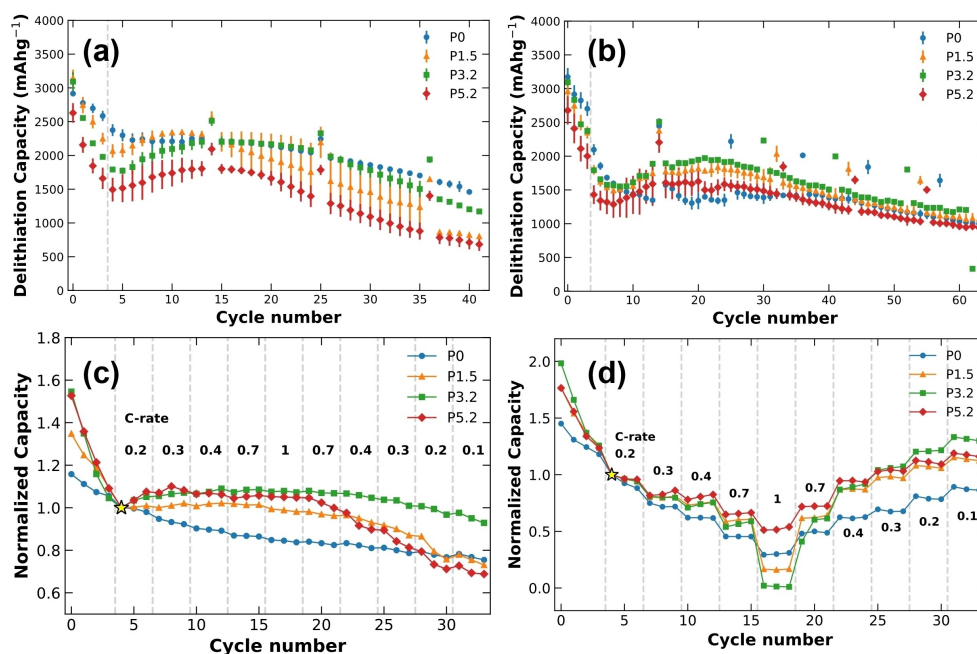


**Figure 3.** Cyclic stability and rate capability behaviour using asymmetric GCD. (a) Cyclic stability with delithiation set to 0.3 C and lithiation set to 0.1 C. (b) Cyclic stability with lithiation set to 0.3 C and delithiation set to 0.1 C. Error bars were calculated from the average of three cells. (c) Normalized delithiation rates with slow lithiation at 0.1 C. (d) Normalized lithiation rates with slow delithiation at 0.1 C. A diagnostic cycle at 0.05 C was included after every tenth cycle for the tests shown in the panels a and b. The star at cycle four in panels c and d is the normalization point, the first point after formation.

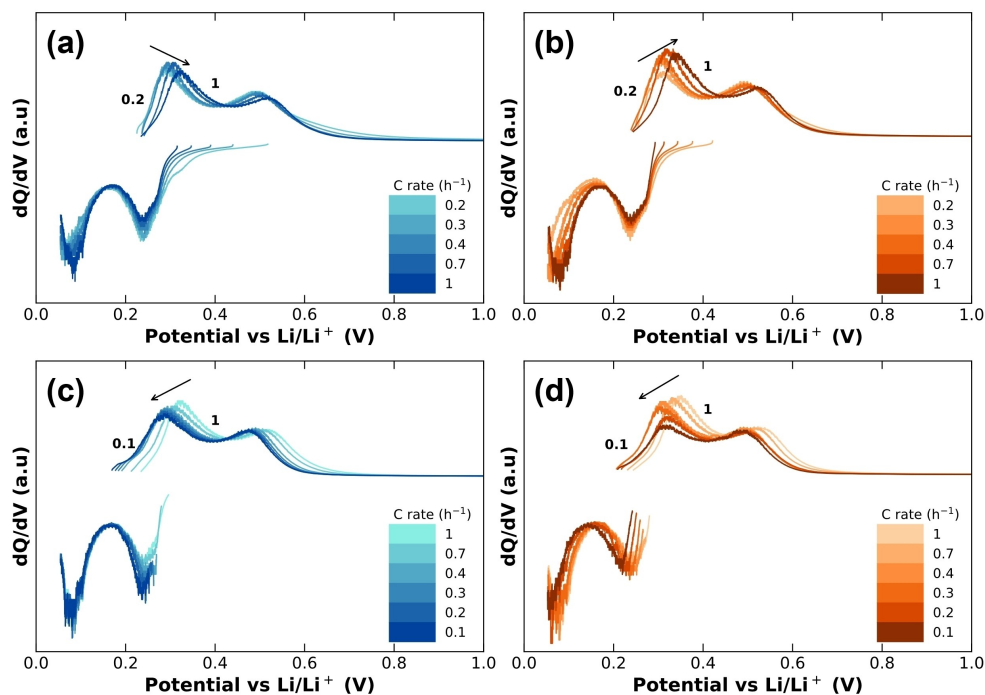


Figure 4. dQ/dV of rate capability experiments with lithiation rate fixed at 0.1 C and varying delithiation rates. (a, b) increasing C-rate; (c, d) decreasing C-rate. (a, c) sample P0; (b, d) sample P1.5.

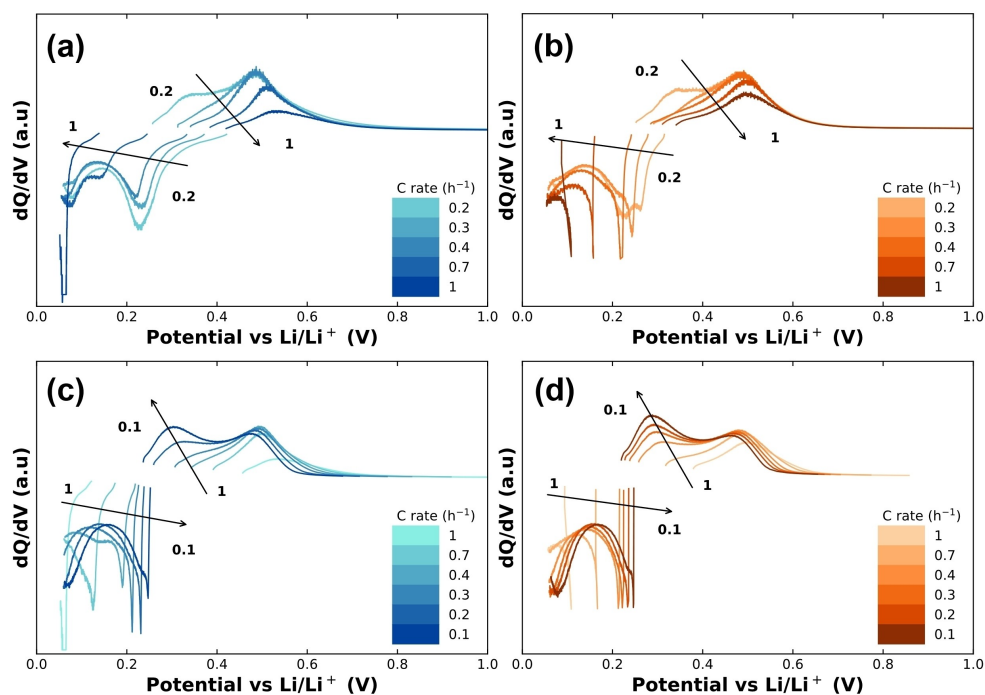


Figure 5. dQ/dV of rate capability experiments with delithiation rate fixed at 0.1 C and varying lithiation rates. (a, b) increasing C-rate; (c, d) decreasing C-rate. (a, c) sample P0; (b, d) sample P1.5.

show the changes in dQ/dV as a function of current for the delithiation and lithiation rate capability tests, respectively.

From Figures 4a and 4b, as the C-rate is increased the delithiation curve (most notably the Li<sub>3.5</sub>Si peak at ~0.28 V) is shifted towards higher potentials – and when the C-rate is

reduced (Figures 4c and 4d), this trend reverses. This potential shift agrees with the expectation that the overpotential increases with the applied current, leading to a shift of the dQ/dV peaks. The reversal of this trend when decreasing the C-rate indicates that there is no significant change in impedance resulting from changing the current of the delithiation step while keeping the lithiation step fixed. Comparing the  $\text{Li}_{3.5}\text{Si}$  peaks in Figures 4a and 4b, it can be seen that the presence of P causes an increase in the size of  $\text{Li}_{3.5}\text{Si}$  peak. This indicates that the capacity of this phase is increasing in the first few cycles, behaviour which is not seen for P0. The behaviour of the  $\alpha\text{-Li}_{2.0}\text{Si}$  peak is almost identical between Si and  $\text{SiP}_x$ , and so this phase can be considered unaffected by the presence of P. The increase in capacity of the  $\text{Li}_{3.5}\text{Si}$  peak may be due to a decrease in resistance of the cell as a result of increasing  $\text{Li}^+$  diffusivity in the electrode.

Similarly to Figure 4, Figure 5 displays the dQ/dV curves for the lithiation-dependent rate capability. These graphs show a strong correlation between the  $\text{Li}_{3.5}\text{Si}$  peak in the delithiation curve as a function of the lithiation rate. Unlike the behaviour shown in Figure 4, Figures 5a and b show that as the lithiation rate is increased, the  $\text{Li}_{3.5}\text{Si}$  peak is quickly lost, and the  $\text{Li}_{2.0}\text{Si}$  peak is strongly diminished. When decreasing the lithiation rate (Figures 5c and 5d), the  $\text{Li}_{3.5}\text{Si}$  and  $\text{Li}_{2.0}\text{Si}$  peaks are recovered. However, the recovery of the  $\text{Li}_{3.5}\text{Si}$  peak is faster for the  $\text{SiP}_x$  materials, with a discernible peak occurring at 0.4 C for materials containing P, but not until 0.2 C for pristine Si. This means that the presence of P in the materials increases the ability for the  $\text{Li}_{3.5}\text{Si}$  to form during lithiation, and that this effect increases over time. This may be partially due to increased  $\text{Li}^+$  diffusivity of  $\text{SiP}_x$  compared to Si. However, this trend is not proportional to P%, nor does it hold at high lithiation rates. Lithiating at 1 C causes the P1.5 and P3.2 materials to have a lower capacity than P0 – and in the case of P3.2, no capacity at all – which indicates that the overpotential at 1 C is very large.

Differential capacity plots are also used to explore the changes in electrochemistry over time. In the present study, they can be used to monitor the evolution of the GCD curves during and after the formation of the broad peak observed in the stability tests. Figures S7 and S8 show the dQ/dV plots of P0, P1.5, P3.2, and P5.2 for cycles 6 to 14 of the delithiation and lithiation stability tests, respectively, which correspond to the cycles spanning the formation of the broad peaks in the capacity observed in Figures 2a and 2b. The pristine Si in Figure S7a shows only a slight broadening of the  $\text{Li}_{3.5}\text{Si}$  peak during delithiation, and a small decrease in overall height in the lithiation. The shift of the delithiation peaks (notably the  $\text{Li}_{3.5}\text{Si}$  peak) to lower potentials for P1.5 and P3.2 (Figures S7b and S7c, respectively) – as well as the increase in peak intensity show that lithiation of these materials is becoming easier over time. The lack of stability in P5.2 makes it difficult to discern features. This same trend can also be seen in the dQ/dV plots of the lithiation stability (Figure S8). Here, the weak  $\text{Li}_{3.5}\text{Si}$  peak grows strongly between cycles 6 to 14 and the overpotential decreases, but only for materials containing P. The  $\text{Li}_{3.5}\text{Si}$  peak in pristine Si decreases and shifts to higher overpotentials over

the same interval. This explains the increase in capacity seen in Figures 3a and 3b.

The behaviour seen in the cyclic stability and rate capability can be summarized thus:

1. The presence of P causes a decrease in overpotential coupled with a slow change in capacity.
2. The P-dependent effect that increases the rate capability forms slowly in the lithiation process.

During cycling we can expect reactions between P, Si and Li to occur, potentially forming small quantities of e.g.  $\text{Li}_3\text{P}$  or  $\text{Li}_2\text{SiP}_2$  (or other, more complicated phosphidosilicates). These chemical species have been shown to form in  $\text{SiP}$  and  $\text{SiP}_2$ , and similar conversions exist in  $\text{SiN}_x$ .<sup>[20,21,23]</sup> It has been shown that these species increase the  $\text{Li}^+$  diffusivity, and it can be hypothesised that their presence may help to explain the results observed.<sup>[26]</sup>

However, the low concentration of P in the  $\text{SiP}_x$  materials studied here means that directly finding these P species via a method such as FTIR or XRD would be difficult. XPS experiments performed on P5.2 electrodes before and after formation the P 2p peak confirms that P is in the  $\text{SiP}_2$  state (Figure S9).<sup>[21]</sup> Unfortunately, due to the low concentration of P it is not possible to conclude that  $\text{Li}_3\text{P}$  or phosphidosilicate species are formed in  $\text{SiP}_x$ . While XPS could potentially be used to determine how P evolves upon cycling, this would require a more dedicated study.

We have employed DFT/AIMD to test whether the P atoms in pristine  $\text{SiP}_x$  will affect the lithiation, and GITT and EIS to test the diffusivity and to find evidence that the P-containing materials have increased  $\text{Li}^+$  ion mobility over pure Si.

### DFT and AIMD on $\text{SiP}_x$ and Si

To better understand the discrepancy between the different materials, it is necessary to explore the behaviour of Li atoms in close proximity to P atoms in the  $\text{SiP}_x$  system. To do this, DFT simulations were performed to calculate the Li behaviour in 64-atom Si systems containing 1, 2, or 3 P atoms. The results are summarized in Table S1, which illustrates that as the concentration of P increases via substitution of Si, so does the energy of the system. This result indicates that inserting relatively high concentrations of P into Si is thermodynamically unfavourable, at least in the low P concentration range. Interestingly, the Li insertion energy displays a local minimum at 1.6 at% P ( $\text{Si}_{63}\text{P}$ ). An AIMD simulation was also performed to evaluate the stability of these systems (shown in Figure S11). As shown in Figure S10a-c, the total energy of each of the  $\text{Si}_{64}$ ,  $\text{Si}_{63}\text{P}$ , and  $\text{Si}_{62}\text{P}_2$  (0, 1.6 and 3.1 at% P, respectively) system is oscillating during the whole MD simulation, whereas the  $\text{Si}_{61}\text{P}_3$  (4.7 at% P, Figure S11d) system shows a remarkable change in total energy. Here one of the Li atoms shifts to neighbouring site, implying that a high P concentration will have a negative effect on lithiation and delithiation behaviour during the charge-discharge process. This “rejection” of Li in proximity to the P may explain why the broad peak in the  $\text{SiP}_x$  exists in Figures 2c and 2d, and also why the effect is stronger for higher concentrations of P.

Higher substitution energy will increase the thermodynamic instability. Lower Li insertion energy will also increase the rate capability during lithiation. The interplay between lower insertion energy and higher thermodynamic instability implies that materials with lower concentrations of P should show good rate capability as well as decent stability, both of which are supported by the experimental data.

### GITT and EIS of SiP<sub>x</sub> and Si

To validate the rate behaviour of these materials, it is necessary to study the Li<sup>+</sup> ion mobility in the materials. The diffusivity  $D_{Li^+}$  of Li<sup>+</sup> in the electrode can be calculated from GITT data from the following equation:<sup>[2,47–49]</sup>

$$D_{Li^+}^{GITT} = \frac{4}{\pi\tau} \left( \frac{m_B V_M}{M_B S} \right)^2 \left( \frac{\Delta E_s}{\Delta E_t} \right)^2 \quad (1)$$

and from EIS using:<sup>[2,45,46]</sup>

$$D_{Li^+}^{EIS} = 1/2 \left[ \left( \frac{V_M}{SFA_W} \right) \left( \frac{\partial E}{\partial x} \right) \right]^2 \quad (2)$$

Where  $\tau$  is the duration of the titration step;  $m_B$  and  $M_B$  are the molecular mass and weight of Si, respectively;  $\Delta E_s$  and  $\Delta E_t$  are the changes in equilibrium and rest potentials, respectively;  $S$  is the area of the electrode;  $F$  is Faraday's constant;  $A_W$  is the Warburg impedance; and  $\partial E/\partial x$  is the local slope of the open circuit potential (OCP) curve. The diffusivity of the lithiation process determined by GITT is given in Figure S12, along with typical examples of the GITT and EIS curves, and the equivalent circuit used for fitting the EIS data.

Figure 6 shows a comparison between the Li<sup>+</sup> ion diffusivity of the materials as calculated from GITT as a function of voltage (Figure 6a) and EIS (Figure 6b) using equations 1 and 2, respectively. Both these figures show that the diffusivity of Li<sup>+</sup> in SiP<sub>x</sub> is significantly greater than for pristine Si even accounting for changes in diffusivity as a result of particle size differences, which would lead to a roughly 2-fold increase in diffusivity of the smallest particles (P5.2) over the largest (P0). The remaining diffusivity increase is then possibly due to the presence of lithium phosphidosilicates hypothesised earlier.

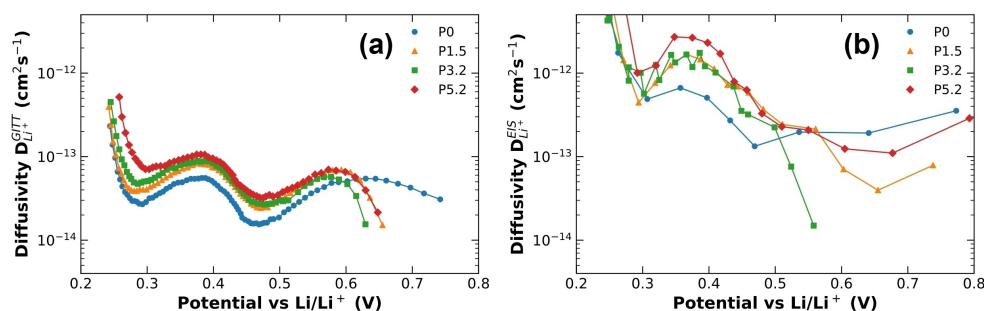


**Figure 6.** Diffusivity as a function of potential for Si and SiP<sub>x</sub>. (a) Diffusivity calculated from GITT data using Equation 1. (b) Diffusivity calculated from the Warburg constants from EIS data using Equation 2. The diffusivities are calculated at the electrode level.

The difference in diffusivities calculated from GITT and EIS can be explained by the difference in equilibrium states, as the relaxation time for GITT is two hours, while that of EIS is 24 hours. This leads to an increase in the slope of  $\partial E/\partial x$ , and therefore a higher  $D_{Li^+}^{EIS}$ . The GITT technique also assumes that the diffusion is linear rather than radial, which leads to smaller values of diffusivity.<sup>[47]</sup>

### Conclusion

Three silicon nanoparticle materials containing concentrations of P of 1.5, 3.2, and 5.2 at% were synthesised to compare the electrochemical behaviour of SiP<sub>x</sub> to pure Si NPs. To decouple lithiation and delithiation behaviour the charge and discharge steps were performed at asymmetric C-rates. Delithiation was found to be enhanced for SiP<sub>x</sub> at high C-rates compared to pure Si, while the lithiation rate capability was only better for low C-rates. GITT and EIS were used to validate the rate behaviour and showed that the diffusivity of Li<sup>+</sup> in SiP<sub>x</sub> is significantly greater than for pristine Si. A hypothesis is proposed whereby Li<sub>3</sub>P, Li<sub>2</sub>SiP<sub>2</sub> or other phosphidosilicates species formed during cycling could be responsible for the increased diffusivity and enhanced delithiation rate in SiP<sub>x</sub>. However, the evidence for this is found to be inconclusive.

### Supporting Information Summary

The supporting information contains the experimental section, as well as TEM images and analysis, XRD, EDS, and charge-discharge plots related to the results and discussion of this article. Further details regarding the computational methods can also be found in the supporting information.

### Acknowledgements

The authors would like to thank the Norwegian Research Council and Beyond AS for the financial support of this project under project No. 304644. Funding support for the manufacturing of particles was provided by the Regional Research Fund of Vestland, Norway under Project No. 299410.

## Conflict of Interest

F. T. Huld, O. E. Eleri, R. Batmaz and F. Lou are employees of Beyonder, a Norwegian battery manufacturing company. F. T. Huld and F. Lou also own stock in Beyonder. The remaining authors declare no conflict of interest.

## Data Availability Statement

Research data are made available on request.

**Keywords:** Li-ion batteries · Silicon phosphorus alloy · nanoparticles · rate capability · Density functional theory

- [1] Y. Liu, R. Zhang, J. Wang, Y. Wang, *iScience* **2021**, *24*, 102332.
- [2] K. Pan, F. Zou, M. Canova, Y. Zhu, J.-H. Kim, *J. Power Sources* **2019**, *413*, 20–28.
- [3] C. K. Chan, R. Ruffo, S. S. Hong, Y. Cui, *J. Power Sources* **2009**, *189*, 1132–1140.
- [4] P. Li, G. Zhao, X. Zheng, X. Xu, C. Yao, W. Sun, S. X. Dou, *Energy Storage Mater.* **2018**, *15*, 422–446.
- [5] M. N. Obrovac, *Curr. Opin. Electrochem.* **2018**, *9*, 8–17.
- [6] J. P. Pender, G. Jha, D. H. Youn, J. M. Ziegler, I. Andoni, E. J. Choi, A. Heller, B. S. Dunn, P. S. Weiss, R. M. Penner, C. B. Mullins, *ACS Nano* **2020**, *14*, 1243–1295.
- [7] V. Vanpeene, J. Villanova, A. King, B. Lestriez, E. Maire, L. Roué, *Adv. Energy Mater.* **2019**, *9*, 1803947.
- [8] A. Funabiki, M. Inaba, Z. Ogumi, S. Yuasa, J. Otsuji, A. Tasaka, *J. Electrochem. Soc.* **1998**, *145*, 172–178.
- [9] K. Persson, V. A. Sethuraman, L. J. Hardwick, Y. Hinuma, Y. S. Meng, A. van der Ven, V. Srinivasan, R. Kostecki, G. Ceder, *J. Phys. Chem. Lett.* **2010**, *1*, 1176–1180.
- [10] X. Shen, Z. Tian, R. Fan, L. Shao, D. Zhang, G. Cao, L. Kou, Y. Bai, *J. Energy Chem.* **2018**, *27*, 1067–1090.
- [11] R. Teki, M. K. Datta, R. Krishnan, T. C. Parker, T.-M. Lu, P. N. Kumta, N. Koratkar, *Small* **2009**, *5*, 2236–2242.
- [12] Z. Jiao, Y. Gao, S. Liu, S. Huang, Y. Jiang, Z. Chen, B. Zhao, *Electrochim. Acta* **2018**, *283*, 1702–1711.
- [13] R. Batmaz, F. M. Hassan, D. Higgins, Z. P. Cano, X. Xiao, Z. Chen, *J. Power Sources* **2018**, *407*, 84–91.
- [14] M. Ge, J. Rong, X. Fang, C. Zhou, *Nano Lett.* **2012**, *12*, 2318–2323.
- [15] O. Salihoglu, Y. E. Kahlout, *Mat. Res.* **2019**, *22*, e20180303.
- [16] J.-H. Noh, K.-Y. Lee, J.-K. Lee, *Trans. Nonferrous Met. Soc. China* **2009**, *19*, 1018–1022.
- [17] M. Ge, J. Rong, X. Fang, A. Zhang, Y. Lu, C. Zhou, *Nano Res.* **2013**, *6*, 174–181.
- [18] K. Roy, M. Wahid, D. Puthusseri, A. Patrike, S. Muduli, R. Vaidhyanathan, S. Ogale, *Sustain. Energy Fuels* **2019**, *3*, 245–250.
- [19] A. Ulvestad, H. F. Andersen, I. J. T. Jensen, T. T. Mongstad, J. P. Mæhlen, Ø. Prytz, M. Kirkengen, *Sci. Rep.* **2018**, *8*, 8634.
- [20] R. Reinhold, D. Mikhailova, T. Gemming, A. B. Missyul, C. Nowka, S. Kaskel, L. Giebeler, *J. Mater. Chem. A* **2018**, *6*, 19974–19978.
- [21] R. Reinhold, U. Stoeck, H.-J. Grafe, D. Mikhailova, T. Jaumann, S. Oswald, S. Kaskel, L. Giebeler, *ACS Appl. Mater. Interfaces* **2018**, *10*, 7096–7106.
- [22] H. Yang, B. Yu, S. Gu, H. Huang, Y. Zhang, D. Liu, X. Zhang, Y. Kang, J. Wang, P. K. Chu, X.-F. Yu, *Nanoscale* **2021**, *13*, 51–58.
- [23] H.-T. Kwon, C. K. Lee, K.-J. Jeon, C.-M. Park, *ACS Nano* **2016**, *10*, 5701–5709.
- [24] T. Chen, J. Wu, Q. Zhang, X. Su, *J. Power Sources* **2017**, *363*, 126–144.
- [25] A. Ulvestad, M. O. Skare, C. E. Foss, H. Krogsæter, J. F. Reichstein, T. J. Preston, J. P. Mæhlen, H. F. Andersen, A. Y. Kopolov, *ACS Nano* **2021**, *15*, 16777–16787.
- [26] S. Strangmüller, H. Eickhoff, D. Müller, W. Klein, G. Raudaschl-Sieber, H. Kirchhain, C. Sedlmeier, V. Baran, A. Senyshyn, V. L. Deringer, L. van Wüllen, H. A. Gasteiger, T. F. Fässler, *J. Am. Chem. Soc.* **2019**, *141*, 14200–14209.
- [27] A. Haffner, T. Bräuniger, D. Johrendt, *Angew. Chem. Int. Ed.* **2016**, *55*, 13585–13588; *Angew. Chem.* **2016**, *128*, 13783–13786.
- [28] M. Miyachi, H. Yamamoto, H. Kawai, T. Ohta, M. Shirakata, *J. Electrochem. Soc.* **2005**, *152*, A2089.
- [29] J. K. Lee, K. B. Smith, C. M. Hayner, H. H. Kung, *Chem. Commun.* **2010**, *46*, 2025.
- [30] S. Chen, L. Shen, P. A. van Aken, J. Maier, Y. Yu, *Adv. Mater.* **2017**, *29*, 1605650.
- [31] S. Y. Lai, J. P. Mæhlen, T. J. Preston, M. O. Skare, M. U. Nagell, A. Ulvestad, D. Lemordant, A. Y. Kopolov, *Nanoscale Adv.* **2020**, *2*, 5335–5342.
- [32] Q. Pan, P. Zuo, T. Mu, C. Du, X. Cheng, Y. Ma, Y. Gao, G. Yin, *J. Power Sources* **2017**, *347*, 170–177.
- [33] G. Li, J.-Y. Li, F.-S. Yue, Q. Xu, T.-T. Zuo, Y.-X. Yin, Y.-G. Guo, *Nano Energy* **2019**, *60*, 485–492.
- [34] B. Long, Y. Zou, Z. Li, Z. Ma, W. Jiang, H. Zou, H. Chen, *ACS Appl. Energy Mater.* **2020**, *3*, 5572–5580.
- [35] S. Huang, L.-Z. Cheong, D. Wang, C. Shen, *ACS Appl. Mater. Interfaces* **2017**, *9*, 23672–23678.
- [36] C.-B. Chang, C.-Y. Tsai, K.-T. Chen, H.-Y. Tuan, *ACS Appl. Energy Mater.* **2021**, *4*, 3160–3168.
- [37] Y. Domi, H. Usui, M. Shimizu, Y. Kakimoto, H. Sakaguchi, *ACS Appl. Mater. Interfaces* **2016**, *8*, 7125–7132.
- [38] H. F. Andersen, W. Filtvedt, J. P. Mæhlen, T. T. Mongstad, M. Kirkengen, A. Holt, *ECS Trans.* **2014**, *62*, 97–105.
- [39] R. Körner, M. P. M. Jank, H. Rysse, H.-J. Schmid, W. Peukert, *J. Aerosol Sci.* **2010**, *41*, 998–1007.
- [40] X. H. Liu, L. Zhong, S. Huang, S. X. Mao, T. Zhu, J. Y. Huang, *ACS Nano* **2012**, *6*, 1522–1531.
- [41] S. Martinet, in *Nanomaterials for Sustainable Energy* (Ed.: Q. Li), Springer Cham, **2016**, p. 471–512.
- [42] C. Keller, A. Desrués, S. Karuppiah, E. Martin, J. Alper, F. Boismain, C. Villeveuille, N. Herlin-Boime, C. Haon, P. Chenevier, *Nanomaterials* **2021**, *11*, 307.
- [43] K. Ogata, E. Salager, C. J. Kerr, A. E. Fraser, C. Ducati, A. J. Morris, S. Hofmann, C. P. Grey, *Nat. Commun.* **2014**, *5*, 3217.
- [44] M. N. Obrovac, L. Christensen, *Electrochem. Solid-State Lett.* **2004**, *7*, A93.
- [45] V. A. Sethuraman, V. Srinivasan, J. Newman, *J. Electrochem. Soc.* **2013**, *160*, A394–A403.
- [46] C. E. L. Foss, S. Müssig, A. M. Svensson, P. J. S. Vie, A. Ulvestad, J. P. Mæhlen, A. Y. Kopolov, *Sci. Rep.* **2020**, *10*, 13193.
- [47] E. Deiss, *Electrochim. Acta* **2005**, *50*, 2927–2932.
- [48] W. Weppner, R. A. Huggins, *Annu. Rev. Mater. Sci.* **1978**, *8*, 269–311.
- [49] C. Ho, I. D. Raistrick, R. A. Huggins, *J. Electrochem. Soc.* **1980**, *127*, 343–350.
- [50] M. Murbach, B. Gerwe, N. Dawson-Elli, L. Tsui, *JOSS* **2020**, *5*, 2349.

Submitted: August 2, 2022

Accepted: October 19, 2022